

Two nondimensional parameters for characterizing the nuclear morphology

Sreenath Balakrishnan,^{1,*} Shilpa. R. Raju,² Anwesha Barua,³ Reshma P. Pradeep,⁴ and Gondi Kondaiah Ananthasuresh^{2,3}

¹School of Mechanical Sciences, Indian Institute of Technology Goa, Goa, India; ²Mechanical Engineering, Indian Institute of Science, Bengaluru, Karnataka, India; ³BioSystems Science and Engineering, Indian Institute of Science, Bengaluru, Karnataka, India; and ⁴School of Physical Sciences, Indian Institute of Science Education and Research Thiruvananthapuram, Thiruvananthapuram, Kerala, India

ABSTRACT Nuclear morphology is an important indicator of cell function. It is regulated by a variety of factors such as the osmotic pressure difference between the nucleoplasm and cytoplasm, cytoskeletal forces, elasticity of the nuclear envelope and chromosomes. Nucleus shape and size are typically quantified using multiple geometrical quantities that are not necessarily independent of one another. This interdependence makes it difficult to decipher the implications of changes in nuclear morphology. We resolved this by analyzing nucleus shapes of populations for multiple cell lines using a mechanics-based model. We deduced two independent nondimensional parameters, namely, flatness index and isometric scale factor. We show that nuclei in a cell population have similar flatness but variable scale factor. Furthermore, nuclei of different cell lines segregate according to flatness. Cellular perturbations using biochemical and biomechanical techniques suggest that the flatness index correlates with actin tension and the scale factor anticorrelates with elastic modulus of nuclear envelope. We argue that nuclear morphology measures such as volume, projected area, height etc., are subsumed by flatness and scale factor, which can unambiguously characterize nuclear morphology.

SIGNIFICANCE The nucleus is shaped by forces from the cytoskeleton and elastic properties of the nuclear envelope, which are conferred by their constituent proteins that include actin, myosin, microtubules, and lamins. The variation in these factors among individual cells in a cell population leads to variability in nuclear morphology. We characterize the physical consequences of this in terms of two easily measurable geometric parameters. We also show that flatness index of nuclei is maintained in a cell population, whereas the scale factor is variable. Any changes in these parameters may therefore be construed as a perturbation to the cell population. Mere measurement of volume and projected area and an analytical formula thus enable detecting a perturbation.

INTRODUCTION

Nucleus morphology is an important indicator (1) and regulator (2) of cell function. Many diseases such as cancer (3,4) and laminopathies (5–7) are known to alter nuclear shape and some of these pathologies can even be diagnosed from these morphological aberrations. An interesting observation about nuclear morphology is the remarkable uniformity in shape but variability in size among individual cells in a population and across multiple cell types. Nuclei of many cell types cultured on two-dimensional substrates have a flat, pancake-like shape (8). It is common practice to use general

measures of geometry such as eccentricity, height, projected area, surface area, and volume for characterizing nuclear morphology (9). One shortcoming of such general shape descriptors is that alterations to nuclear morphology cannot be easily attributed to specific cellular perturbations. For instance, increasing extracellular osmolarity reduced height, projected area, and volume (10), whereas increasing substrate elasticity increased projected area, reduced height, and did not change the volume (11,12). These observations suggest that the information regarding the mechanism of nuclear shape change is contained in a combination of these nuclear parameters and not in a single parameter. Here, we identify alternate canonical nuclear morphology measures by analyzing the variability in nuclear morphology across multiple cell types using a mechanical model.

The simplest mechanical model for a pancake-like geometry is an inflated membrane compressed between

Submitted November 16, 2020, and accepted for publication September 15, 2021.

*Correspondence: sreenath@iitgoa.ac.in

Editor: Vivek Shenoy.

<https://doi.org/10.1016/j.bpj.2021.09.035>

© 2021 Biophysical Society.

two rigid plates (Fig. 1 C) (8). Inflating pressure is the net pressure due to the osmotic pressure difference between the nucleoplasm and cytoplasm and the compression from microtubules. The compressive force from the flat rigid plate on the top is due to the cortical actin tension and the bottom rigid plate is the cell substrate. Even though the compressive force from actin tension would be akin to the compressive force from a stretched membrane, we have assumed a flat plate. This assumption is tenable because the cell area is typically much larger than the nuclear area. By using the mechanical analysis developed in (13) for such a mechanical configuration (Fig. 1 C), we obtained two sets of interrelated nondimensional parameters that can describe nuclear morphology:

- 1) $\eta_1 = PR/2E_1H$, the ratio between the expanding pressure, P , to the elastic modulus of the nuclear envelope, E_1 . R and H are the radius and thickness, respectively, of the nuclear envelope in the undeformed state (Fig. 1 B), and $\eta_2 = \sqrt{F/P\pi R^2}$, the ratio between the compressive force, F , to P and
- 2) λ_0 (scale factor), the elastic stretch at the apex of the nucleus, and τ (flatness index), half of the angle subtended by cortical actin on the nuclear envelope in the undeformed state (Fig. 1 B).

η_1 and λ_0 represent the effect of P and E_1 on nucleus morphology. P expands the nucleus, which is resisted by E_1 . Therefore, when E_1 increases, η_1 and λ_0 decrease, and vice versa. η_2 and τ indicate the effect of cortical actin tension by quantifying the contact area between the cortical actin and the nuclear envelope in the model (orange region in Fig. 1 C). η_2 is the ratio between the radius of this contact region to the radius of the undeformed state: $M'N'/R$ (Fig. 1 C). When this contact region is mapped to the undeformed configuration (orange region in Fig. 1 B), it can be characterized by the angle subtended at the center, τ (Fig. 1 B). Higher actin tension will flatten the nucleus, increasing this contact area, and thereby increasing η_2 and τ .

It may be noted that our model has only two independent parameters and hence the values of any one set of nondimensional parameters can be estimated from the other (Fig. 1 D). For instance, $\lambda_0 \approx M'N'/MN = (\eta_2 R)/(\tau R) \Rightarrow \eta_2 \approx \lambda_0 \tau$ where τ is in radians. These parameters can be obtained by fitting our model to nuclear shape. Because there are only two independent nondimensional parameters, we need only two geometric parameters of the nucleus to fit our model. Any other geometric parameter can then be computed from the model. For example, we can predict the surface area of the nucleus if we know its projected area and volume. This relationship among projected area, volume, and surface area is represented by a surface in the three-dimensional (3D) space

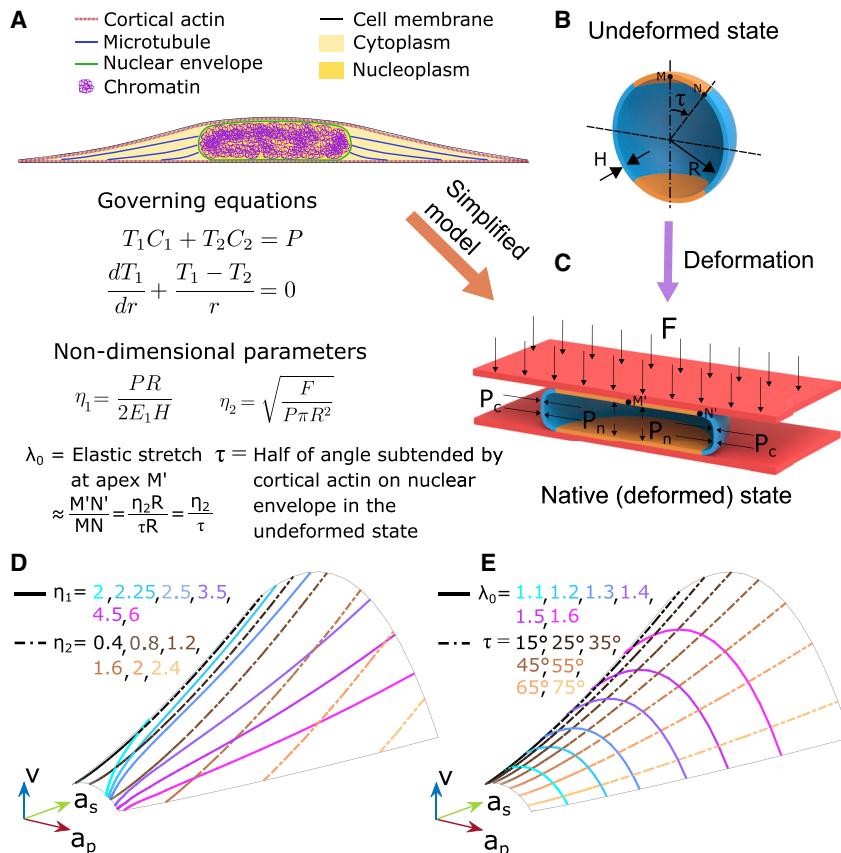


FIGURE 1 Two-parameter nondimensional model for nucleus morphology. (A) Nuclear envelope (green) is shaped by forces from cortical actin (orange), microtubules (blue), chromatin (purple), and an osmotic pressure difference between the nucleoplasm and cytoplasm. (B) The reference configuration, undeformed state, of the nuclear envelope is assumed to be a spherical membrane of radius R and thickness H . (C) Forces from osmotic pressure, microtubules, and chromatin is lumped into an inflating pressure $P = P_n - P_c$. The force due to cortical actin, F , is assumed to be akin to a rigid flat plate pushing down on the nucleus. The equations of equilibrium of the nuclear envelope in terms of principal tensions, T_1 and T_2 , and principal curvatures, C_1 and C_2 , are shown. Solutions to these equations depend on two nondimensional parameters. Two choices for these nondimensional parameters are 1) η_1 and η_2 , and 2) λ_0 and τ . By simulating the model for various values of these nondimensional parameters, we obtained the corresponding nuclear shapes. Normalized projected area (a_p), surface area (a_s) and volume (v), estimated from these nuclear shapes formed a surface in the a_p - a_s - v space because there are only two independent nondimensional parameters governing them. The contour lines of the nondimensional parameters, η_1 and η_2 (D), and λ_0 and τ (E), on this surface are shown. To see this figure in color, go online.

defined by these geometric parameters (Fig. 1, *D* and *E*). The projected area, surface area and volume are normalized (represented by a_p , a_s , and v , respectively in Fig. 1, *D* and *E*) with the radius of the undeformed configuration, R (see [Materials and methods](#)), to account for the variability in nuclear size among different cell lines. R is different for different cell lines but constant for all cells in a population. For every point on this surface the corresponding nondimensional parameters, η_1 , η_2 , λ_0 , and τ can be obtained by fitting our model to a_p , a_s , and v corresponding to that point. The relationship among the geometric parameters, a_p , a_s , and v , and the nondimensional parameters, η_1 , η_2 , and λ_0 , τ , is shown using contour lines on this surface (Fig. 1, *D* and *E*). Previously, we had used this model to infer molecular mechanisms responsible for changes in nuclear mechanics due to hepatitis C virus by analyzing the changes in nuclear morphology (14). In that work, we had used η_1 and η_2 , which are expressed in terms of mechanical parameters such as P , E_1 , and F . Here, we identified that τ and λ_0 align with the principal directions of variability in nuclear shapes and hence form a canonical basis for nuclear morphology. Furthermore, using cellular perturbations, we identify the geometric and physical interpretations of these parameters.

We first verified the applicability of our model to multiple cell lines by testing the relationship among different geometric parameters predicted by our model (Fig. 1, *D* and *E*). For this, we measured nuclear volume, surface area, and projected area of individual nuclei from multiple cell lines using confocal imaging. For all the cell lines, these nuclear geometric parameters lie on the surface predicted by our model, confirming the applicability of our model to individual nuclei. Furthermore, nuclei from a given cell population lie on a straight line on the surface. The location and orientation of the line on the surface varies with cell type. By using our model, we show that the orientation of this line is along λ_0 . Next, we investigated the changes in these nondimensional parameters using cellular perturbations. We depolymerized actin using cytochalasin D, depolymerized microtubules using nocodazole, and cultured cells on polyacrylamide gels of varying elastic moduli. We found that τ correlates with actin tension and λ_0 anticorrelates with the elastic modulus of the nuclear envelope. By using the model, we further obtained the geometric interpretations of τ and λ_0 as the flatness and isometric scaling of the nucleus, respectively. Previous studies that have quantified nuclear flatness by measuring its height and projected area also indicate that τ correlates with actin tension. Finally, we derive a convenient method for estimating τ from nuclear area and volume using an analytical expression and a graph.

MATERIALS AND METHODS

Cell culture, chemical treatments, and immunofluorescence

All cell lines were cultured at 37°C in DMEM with 10% FBS. Cells were regularly passaged at around 80% confluence. For the cytochalasin D and no-

codazole treatments, cells were seeded at low concentrations, around 100 k cells on a 22-mm circular coverslip (Blue Star), and allowed to attach overnight. 16 h after seeding, the cell medium was replaced with another containing the chemical at the required concentration for 2 h. For our studies we have used 0.46 and 0.92 μ M solutions of cytochalasin D and 6 μ M solution of nocodazole in DMEM. After incubation for 2 h, the cells were fixed using 4% paraformaldehyde and stained for nucleus and actin using Hoechst 33342 (Thermo Fisher Scientific, Waltham, MA) and rhodamine phalloidin (Thermo Fisher Scientific), respectively. Confocal z stacks of the stained cells were taken on a Leica Microsystems TCS SP5 II confocal microscope. An oil-immersion objective lens with a magnification of 63 \times and a numerical aperture of 1.4 was used. Z stack images were taken at a pixel size of 240 nm in the lateral directions and z -step size of 500 nm. The morphology of the nucleus was obtained from these confocal stacks using a 3D-active-contour-based image processing technique developed previously (14).

Polyacrylamide gel fabrication and characterization

We have followed the protocol for polyacrylamide gel fabrication reported in (15). Coverslips were ultrasonicated in 10% Extran solution for 15 min and kept in hot-air oven at 80°C for 30 min. The coverslips were then washed with de-ionised (DI) water and the traces of water were removed by rinsing with 100% ethanol. The cleaned coverslips were then kept overnight for drying at 80°C in the hot-air oven. For better adhesion to gels, these coverslips were activated by treating with 10% 3-(aminopropyl)-triethoxysilane for 15 min and subsequently washed with DI water and treated with 0.5% glutaraldehyde for 30 min. The coverslips were washed again and dried in the laminar air-flow hood and sterilized using ultraviolet rays (UV).

We fabricated three bioinert polyacrylamide gels of different elastic moduli, low, intermediate, and high, by altering the relative concentrations of acrylamide monomer and bis-acrylamide cross-linking monomer. Polyacrylamide gel precursors were prepared by mixing 10% v/v acrylamide (40%; Sigma-Aldrich) with 0.03%, 0.1%, and 0.3% v/v of N,N'-methylenebisacrylamide (bis-AA 2% w/v in DW; Sigma) in DI water for low, intermediate, and high elastic modulus gels, respectively. Gelation was initiated by adding 0.1% v/v tetramethylethylenediamine (Sigma-Aldrich) and 0.1% w/v ammonium persulfate (Sigma-Aldrich) to the gel precursor. 30 μ L of this solution was pipetted to silanized coverslips, covered with extran-treated glass slides and cured for 30 min. The coverslip with the intact gel was carefully peeled off from the glass slide. Next, we treated these gels with Sulpho-SANPAH to enable cell adhesion. Gels were immersed in 1 mg/mL sulfo-SANPAH (Thermo Fisher Scientific) in 50 mM (pH 8.5) HEPES and reacted under UV for 10 min. The treated gels were washed thrice with HEPES buffer. To improve cell adhesion, we coated the gels with collagen. Rat tail collagen-I was mixed in 0.1 M acetic acid (Thermo Fisher Scientific) at equal volume and in 50 mM (pH 8.5) HEPES to reach 0.1 mg/mL final concentration. Gels were immersed in this collagen solution and incubated overnight at 4°C. Before cell seeding, the gels were sterilized by UV inside the laminar air-flow hood for 20 min. The gels were maintained in a hydrated state all throughout these steps.

The elastic modulus of the gels were determined using an Atomic Force Microscope (XE Bio from Park Systems, Suwon, South Korea). We have used a V-shaped cantilever with a spherical bead of diameter 5.2 μ m made of silicon dioxide attached to its bottom (AppNano HYDRA6V-200NG-TL; AppNano, Mountain View, CA). The force-displacement curves were fit to a Hertzian contact model to determine the elastic modulus (14). We obtained the following elastic moduli for the gels: low = 2.5 ± 0.3 kPa, intermediate = 10.7 ± 0.2 kPa, and high = 36 ± 2.2 kPa.

Nondimensional mechanical model for the nucleus

We assumed that the nucleus is shaped by two forces, an expanding pressure, P , and a downward compressive force, F (8). Forces on the nuclear

envelope from 1) osmotic pressure difference between the nucleoplasm and cytoplasm, 2) compression in microtubules, and 3) chromatin were lumped into an inflating pressure, P (16). The compressive force is the downward force due to cortical actin and was assumed to be akin to a flat rigid plate pushing down on the nuclear envelope (8). The nuclear envelope was assumed to be a hyperelastic membrane (incompressible Mooney-Rivlin material) that is spherical in the unloaded state (8,16,17).

Because the initial geometry, forces and boundary conditions are axisymmetric, we used an analytical formulation developed for mechanical equilibrium of axisymmetric membranes (13). The solution to the governing equations for these boundary conditions depend only on two nondimensional parameters, 1) $\eta_1 = PR/2E_1H$ and 2) $\eta_2 = \sqrt{F/P\pi R^2}$, where P is the expanding pressure, E_1 is the elastic modulus of the nuclear envelope, F is the compressive force from cortical actin, R is the radius, and H is the thickness of the nuclear envelope in the undeformed state. η_1 appears in the governing equation, and η_2 comes from the boundary condition. For solving these differential equations, we require two other parameters: 1) λ_0 , the stretch at the apex point of the nuclear envelope (point M' in Fig. 1 C) and 2) τ , half of the angle subtended by the contact region between cortical actin and nuclear envelope in the undeformed state (Fig. 1 B). However, as there are only two independent parameters, by specifying either of them, the other two can be determined (14). In our simulations we have specified λ_0 and τ , and estimated η_1 and η_2 .

We first solved the forward problem, i.e., to estimate the nucleus morphology for a given set of nondimensional parameters. For given λ_0 and τ , we first calculated η_1 and η_2 , and then numerically integrated the governing equations to obtain the normalized nuclear morphology, which is the deformed shape when a spherical membrane of unit radius, thickness, and modulus of elasticity are deformed by an inflating pressure = η_1 and compressive force = η_2 . The actual nuclear morphology can be obtained by scaling the normalized nuclear morphology by R . The actual and normalized nuclear geometric parameters are related through the following scaling relations: $A_p = R^2 a_p$, $A_s = R^2 a_s$, and $V = R^3 v$, where A_p , A_s , and V are the actual projected area, surface area, and volume of the nucleus and a_p , a_s , and v are the corresponding normalized quantities.

Next, we used this forward problem to fit our model and obtain nondimensional parameters corresponding to experimentally measured nuclei. We calculated the projected area, surface area, and volume of individual nuclei from the nuclear surfaces obtained by applying our image processing method on the confocal images. These nuclear geometric parameters were normalized using the following relations: $\hat{a}_p = A_p/R^2$, $\hat{a}_s = A_s/R^2$, and $\hat{v} = V/R^3$, where “^” indicates the experimentally measured quantities. The model was fitted to individual nuclei by minimizing the error between the simulated and experimentally measured normalized nuclear morphologies:

$$\min_{\lambda_0, \tau} \left(\frac{a_p - \hat{a}_p}{\hat{a}_p} \right)^2 + \left(\frac{a_s - \hat{a}_s}{\hat{a}_s} \right)^2 + \left(\frac{v - \hat{v}}{\hat{v}} \right)^2.$$

The trust-region-reflective algorithm (18) implemented in the `lsqnonlin` function in MATLAB was used for minimization.

We have considered only those fits in which the error between the model and experimentally measured nuclei was less than 10% for each of the nuclear geometric parameters. More than 90% of nuclei from each experiment were found to fit within this error threshold. Because we have assumed the nuclear envelope as a membrane and neglected bending modulus, it will buckle under compression and therefore $\lambda_0 > 1$. Hence, R was chosen such that more than 90% of the nuclei satisfy this criteria on λ_0 . Nuclei with $\lambda_0 < 1$ were not considered in our analysis. Furthermore, for each experiment, we have used the same R for all the nuclei of a cell line because individual cells of each cell line were assumed to be descendant from a single clone. More details of the model are available in our previous publication (14).

Statistical analyses

For the experiments involving multiple test groups, cytochalasin D treatment and polyacrylamide gels, we have used ANOVA with Bonferroni correction for statistical analysis. All groups which showed statistically significant difference in means, $p < 0.05$, were indicated on the figures. For the experiment with a single test group, nocodazole treatment, we have used Kolmogorov-Smirnov test for statistical analysis.

RESULTS

Variability in nuclear shape

To quantify the variability in nuclear morphology we acquired confocal images of the nuclei of Huh7, HeLa, NIH3T3, MDAMB231, and MCF7 cells. Nuclear surfaces were obtained (Fig. S1) from these confocal images using a 3D-active-contour-based image processing algorithm that we had previously developed (14). From the nuclear surfaces, we calculated the projected area, surface area, and volume of each nuclei. Next, we normalized these geometric parameters (a_p , projected area; a_s , surface area, v , volume) using the radius of the undeformed state, R (see Materials and methods). These normalized geometric parameters were fit to our model to obtain the nondimensional parameters, η_1 , η_2 , λ_0 , and τ , of each nuclei. Our two-parameter model could fit the three nuclear geometric parameters at less than 10% error in each of these parameters, for more than 90% of the nuclei imaged from all cell lines.

The nuclear geometric parameters corresponding to individual nuclei of all cell lines lie on the surface in the a_p - a_s - v space predicted by the model (Fig. 2 A). Furthermore, the geometric parameters corresponding to nuclei from each cell line cluster around straight lines (Fig. 2 A). To obtain the direction of this straight line for each cell line, we calculated the eigenvectors of the covariance matrix of the normalized projected area, surface area, and volume (Fig. 2 B). The largest and second-largest eigenvectors, v_1 and v_2 , respectively, were aligned with λ_0 and τ , respectively (Fig. 2 B). We confirmed this by calculating the Pearson's correlation coefficient of λ_0 and τ with the components of nuclear geometric parameters along the eigenvectors, v_1 and v_2 . λ_0 and τ showed high correlation with v_1 and v_2 , respectively, whereas λ_0 and v_2 , and τ and v_1 were uncorrelated for all cell lines (Table S1). We obtained the standard deviation along the principal directions (σ_1 , σ_2 , and σ_3) by calculating the square root of the eigenvalues (Table 1). σ_1/σ_2 was equal to 9.7, 3.8, 6.2, 6.8, and 5.1 for Huh7, HeLa, NIH3T3, MDAMB231, and MCF7 cells, respectively. The large value of this ratio shows that the variability in nuclear shapes is mostly along one direction, i.e., along λ_0 . Variability along τ was less than one-fourth of the variability along λ_0 . Hence, nuclear morphology is mostly a single-variable function of λ_0 . Nuclear morphology of HeLa cells obtained from an independent study (19) also exhibited this univariate behavior (last row of Table 1). This was

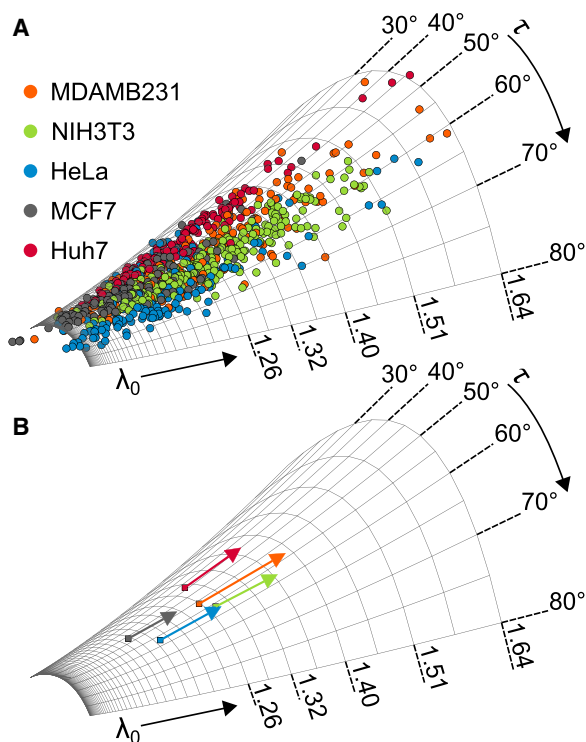


FIGURE 2 Variability in nucleus shape.

For a Figure360 author presentation of this figure, see <https://doi.org/10.1016/j.bpj.2021.09.035>.

(A) Nuclear shape parameters, normalized projected area, surface area, and volume of individual nuclei of MDAMB231 (orange, $N = 204$), HeLa (blue, $N = 173$), MCF7 (gray, $N = 143$), Huh7 (red, $N = 131$), and NIH3T3 (green, $N = 241$) cells plotted over the model surface (B) Direction of largest variability in nucleus shape was obtained by estimating the principal eigenvector of the covariance matrix of normalized projected area, surface area and volume of the nuclei. The length of the arrow is proportional to the square root of the largest eigenvalue. To see this figure in color, go online.

further confirmed by the linear correlation between the other set of nondimensional parameters, η_1 and η_2 (Fig. S2 A). Pearson's correlation coefficient between η_1 and η_2 was 0.69, 0.9, 0.94, 0.9, and 0.89 for Huh7, HeLa, NIH3T3, MDAMB231, and MCF7 cells, respectively. In contrast, λ_0 and τ were uncorrelated (Fig. S2 B). Pearson's correlation coefficient between λ_0 , and τ was -0.04 , -0.26 , 0.30 , 0.17 , and -0.11 for Huh7, HeLa, NIH3T3, MDAMB231, and MCF7 cells, respectively. The alignment of λ_0 and τ with the principal variability of nuclear shapes and their mutual orthogonality suggest that they are a canonical basis for describing nuclear morphology.

Next, we checked if the range of values of λ_0 and τ indicate intrinsic properties of each cell line or whether they represent the mechanical state of the cells. For this, we perturbed the mechanical state of cells by culturing them at a high cell density. τ was significantly lower in high-seeding-density cultures in comparison to those at low-seeding-density (Fig. S3) suggesting that these nondimensional physical parameters were not fundamental properties of the cells, but indicative of their mechanical state. For further

TABLE 1 Principal variability in nuclear morphology

Cell line	Principal variability		
	σ_1	σ_2	σ_3
Huh7	5.6	0.6	0.2
HeLa	5.7	1.5	0.3
NIH3T3	5.6	0.9	0.2
MDAMB231	8.1	1.2	0.4
MCF7	4.6	0.9	0.2
HeLa (19)	3.7	0.4	0.05

Variability of nuclei of HeLa cells from an independent study (19) is given in the last row.

understanding the relationship of these nondimensional parameters with the cell mechanical state, we modulated the cells using biochemical (cytochalasin D and nocodazole) and biomechanical (polyacrylamide gels) mechanisms.

Depolymerizing actin cytoskeleton by treating with cytochalasin D

We systematically depolymerized actin cytoskeleton by treating with increasing concentrations of cytochalasin D, 0.46 and 0.92 μM , on four cell lines: HeLa, MCF7, MDAMB231, and Huh7. Nuclear morphology obtained from confocal images (Fig. S4) were fit to our model to estimate the nondimensional parameters of individual cells (Figs. 3 and S5). τ decreased and λ_0 increased with increasing concentration of cytochalasin D. The reduction in τ could be because of the decrease in F due to actin depolymerization and subsequent decrease in the contact area between the nuclear envelope and cortical actin. Reduction in actin tension has also been shown to reduce lamin-A,C expression, and thereby reduce the modulus of the nuclear envelope (20,21). This would expand the nucleus thereby increasing λ_0 .

In Huh7 cells, the decrease in τ was not significant (Fig. 3 D). We hypothesized that this could be because F is low in Huh7 control cells and hence a further reduction in F due to actin depolymerization did not change the contact area significantly. Low F was indicated by low τ , $\sim 30^\circ$ (Fig. 3 D). At such low τ , the nucleus is approximately spherical and our assumption of representing the force from cortical actin with a rigid flat plate may not be applicable. To test this, we generated cells with approximately spherical nuclei by culturing them at high-seeding-density and then treated them with cytochalasin D (Fig. S6). We confirmed from the images that the nuclei were approximately spherical, which is also indicated by low τ . In such cells, τ did not change consistently with cytochalasin D treatment (Fig. S6) confirming our hypothesis.

Depolymerizing microtubules by treating with nocodazole

Next, we depolymerized microtubules by treating cells with nocodazole. Huh7, MCF7, MDAMB231, and NIH3T3 cells

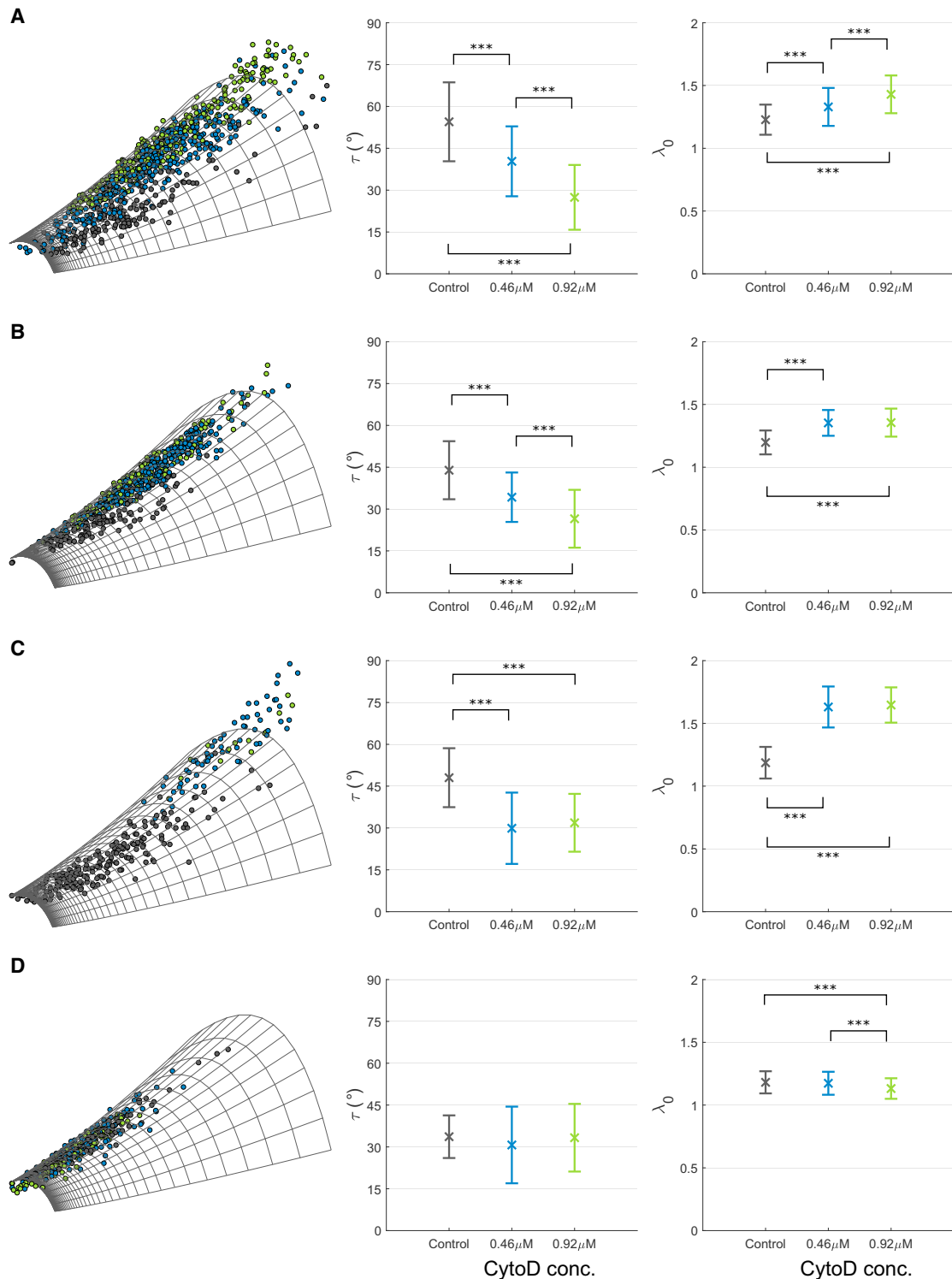


FIGURE 3 Changes in nondimensional parameters due to cytochalasin D treatment. Four cell lines, (A) HeLa ($N_1 = 151$, $N_2 = 293$, $N_3 = 164$), (B) MCF7 ($N_1 = 137$, $N_2 = 239$, $N_3 = 152$), (C) MDAMB231 ($N_1 = 195$, $N_2 = 88$, $N_3 = 22$), and (D) Huh7 ($N_1 = 131$, $N_2 = 159$, $N_3 = 104$) were treated with two concentrations, 0.46 μM , and 0.92 μM of cytochalasin D. Number of nuclei analyzed is represented by $N_1 = \text{control}$, $N_2 = 0.46 \mu\text{M}$, and $N_3 = 0.92 \mu\text{M}$ of cytochalasin D. By fitting our model to individual nuclei, nondimensional parameters λ_0 and τ were estimated. Scatter plot of nuclear shape parameters on the model surface is shown in the left column. Each dot is an individual nucleus, and the colors represent black – control, blue – 0.46 μM , and green – 0.92 μM of cytochalasin D. Bar graphs with the mean and standard deviation of τ and λ_0 are shown in the center and right columns, respectively. Statistical analysis was performed using ANOVA with Bonferroni correction and significance levels are represented by * $p < 0.05$, ** $p < 0.01$, and *** $p < 0.001$. To see this figure in color, go online.

were incubated with 6 μM nocodazole for 2 h. We fit our model to nuclear shapes obtained from confocal images (Fig. S7) and obtained the nondimensional parameters (Figs. 4 and S8). We observed that τ increased significantly in all the cell lines, whereas the variation in λ_0 was lower and inconsistent across cell lines (Fig. 4). Depolymerizing microtubules by nocodazole has been shown to increase actin tension (22,23) via the Rho/ROCK pathway (24–27). This will increase F and the contact area between the cortical actin and nuclear envelope and hence, increase τ . Furthermore, nocodazole treatment abrogates the compressive pressure exerted by microtubules on the nuclear envelope by depolymerizing them (8). This would increase P and λ_0 . On the other hand, enhanced actin tension is known to increase E_1 , by upregulating lamin-A,C (20,21), thereby decreasing λ_0 . These competing mechanisms could have balanced each other and stabilized λ_0 .

Varying substrate stiffness

We further investigated the changes in the nondimensional parameters because of changes in substrate stiffness. Alterations in elastic modulus of the substrate are known to change many cellular properties such as the shape and stiffness primarily because of changes in the cytoskeleton (20,28). Huh7 cells were grown on polyacrylamide gels of 2.5, 11, and 36 kPa elastic moduli. Glass coverslip of elastic modulus ≈ 1 GPa was used as control. We obtained confocal images of individual nuclei (Fig. S9) and estimated the nondimensional parameters by fitting our model (Figs. 5 and S10). We observed that τ increased and λ_0 decreased with increasing substrate elastic modulus (Figs. 5 and S9). Previously, mesenchymal stem cells (MSCs) cultured on polyacrylamide gels of increasing elastic modulus were shown to have enhanced actin tension and lamin-A,C expression (20). This would increase F and increase E_1 , which would, in turn, increase τ and decrease λ_0 .

Geometric interpretation of nondimensional parameters

In all our experiments, we observed that increasing actin tension (nocodazole and substrate stiffness) increased τ and decreasing actin tension (cytochalasin D) decreased τ for all the cell lines. This also corroborates with the physical interpretation of τ as a measure of the contact area between the cortical actin and the nuclear envelope. Higher actin tension flattens the nucleus, thereby increasing the contact area and τ . Hence, we hypothesized that τ is related to the flatness of the nucleus. To test this, we simulated our model for a range of values of τ and λ_0 and estimated the flatness of the nuclear shape obtained. We quantified the flatness using aspect ratio, defined as the ratio of height to diameter. The aspect ratio decreased slightly with λ_0 for $\lambda_0 < 1.2$ and remained constant for $\lambda_0 > 1.2$ for all values of τ

(Fig. 6 A). Aspect ratio decreased with τ for all values of λ_0 (Fig. 6 A). Therefore, τ can be interpreted geometrically as inversely proportional to the aspect ratio. To further confirm this, we calculated the correlation between the aspect ratio and the components of the nuclear geometric parameters along the principal directions of variability (Fig. 1; Table S1). Aspect ratio was negatively correlated with the second principal direction and uncorrelated with the first principal direction. Pearson's correlation coefficient was -0.88 , -0.94 , -0.83 , -0.8 , and -0.94 with the second principal direction, and -0.3 , -0.11 , -0.43 , -0.42 , and -0.1 with the first principal direction for Huh7, HeLa, NIH3T3, MDAMB231, and MCF7 cells, respectively. For a given aspect ratio, the nucleus can scale isometrically, which is represented by λ_0 (Fig. 6 A). The independence of these geometrical transformations, flattening and scaling, is indicated by the orthogonality of τ and λ_0 on the model surface (Fig. 1 E).

We used the anticorrelation between τ and aspect ratio to compare our experimental results with previous studies. Many studies have reported changes in nuclear height and projected area as a consequence of perturbations to cellular and extracellular factors governing nuclear shape. From these measurements, alternations in aspect ratio can be inferred.

- 1) Aspect ratio of nuclei increased when cells were treated with reagents such as latrunculin A (Fig. 1 e in (9)), blebbistatin (Fig. 3 d in (29)), and Y-27632 (Fig. SE10 in (30)), which disrupt the actin cytoskeleton and decrease actin tension. Aspect ratio increased with microtubule stabilization by Paclitaxel, which is also known to decrease actin tension (31,32).
- 2) Aspect ratio of nuclei decreased when *Drosophila* S2R + cells were treated with nocodazole (Fig. 1 e in (9)).
- 3) Aspect ratio of nuclei of MSCs (Fig. 1 in (20)) and NIH3T3 cells (Fig. 1 in (11)) decreased when grown on substrates of increasing elastic moduli.

All these studies independently support our experimental results correlating actin tension with τ .

Finally, we derived a convenient technique to calculate τ from projected area and volume of the nucleus. We observed that the simulated nuclear shapes can be approximated by a flat “pancake” geometry with circular ends (Fig. 6 B). For such geometries, the aspect ratio, γ , can be shown to be the solution of the cubic equation,

$$\left(\frac{5}{3} - \frac{\pi}{2}\right)\gamma^3 - \left(2 - \frac{\pi}{2}\right)\gamma^2 + \gamma - Q = 0, \quad (1)$$

where Q is a nondimensional function of nuclear volume V and projected area A given by $Q = (V\sqrt{\pi})/(2A^{3/2})$ (see Supporting materials and methods for derivation). Analytical expression for the solution of this cubic equation is as follows,

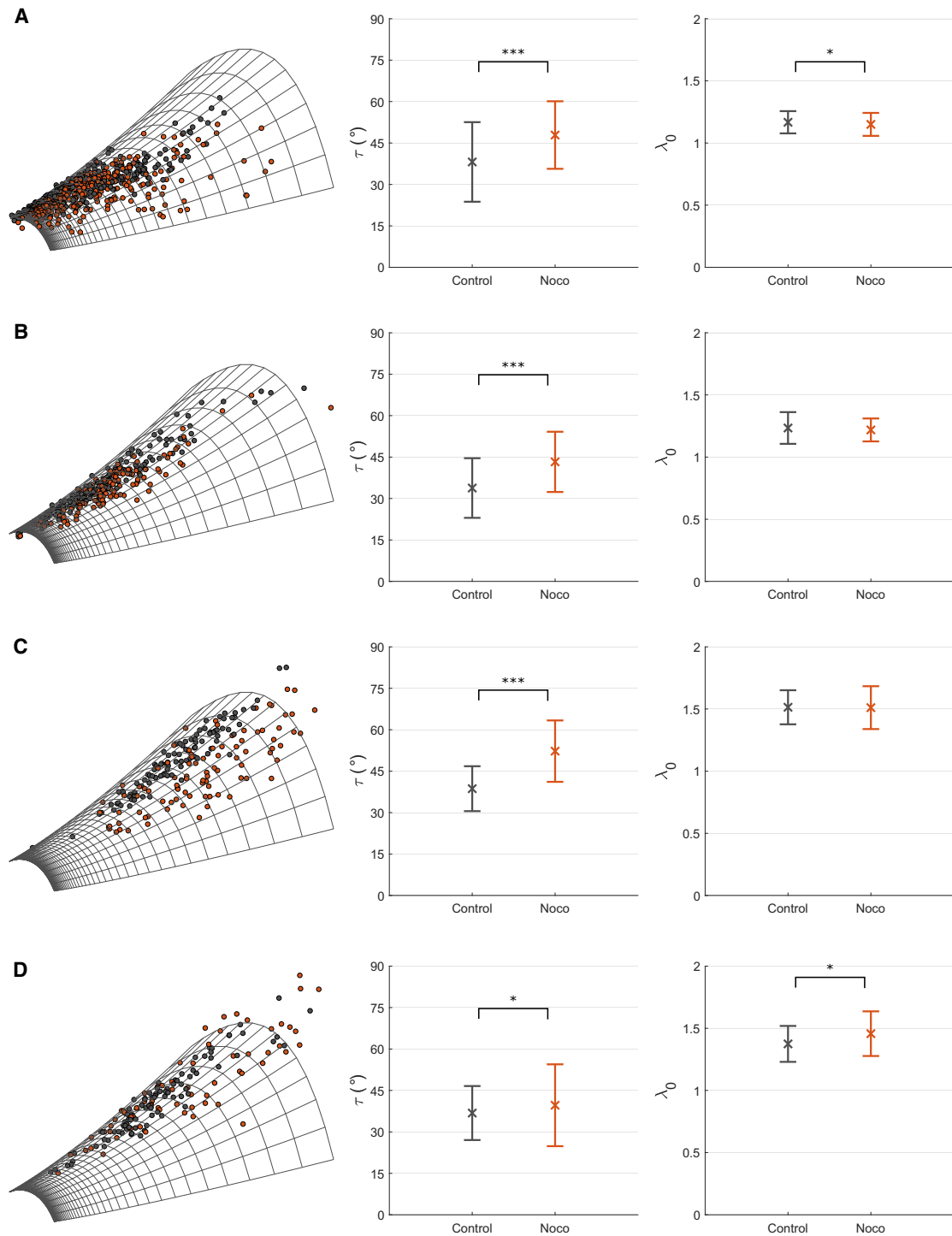


FIGURE 4 Changes in nondimensional parameters due to nocodazole treatment. Four cell lines, (A) Huh7 ($N_1 = 287$, $N_2 = 304$), (B) MCF7 ($N_1 = 127$, $N_2 = 119$), (C) MDAMB231 ($N_1 = 99$, $N_2 = 94$), and (D) NIH3T3 ($N_1 = 81$, $N_2 = 75$), were treated with $6 \mu\text{M}$ nocodazole. Number of nuclei analyzed is represented by $N_1 = \text{control}$, and $N_2 = \text{nocodazole-treated}$. By fitting our model to individual nuclei, nondimensional parameters λ_0 and τ were estimated. Scatter plot of nuclear shape parameters on the model surface is shown in the left column. Each dot is an individual nucleus and the colors represent black–control, and red–nocodazole-treated cells. Mean and standard deviation of τ and λ_0 are shown in the center and right columns respectively. Statistical analysis was performed using Kolmogorov-Smirnov test and significance levels are represented by $*p < 0.05$, $**p < 0.01$, and $***p < 0.001$. To see this figure in color, go online.

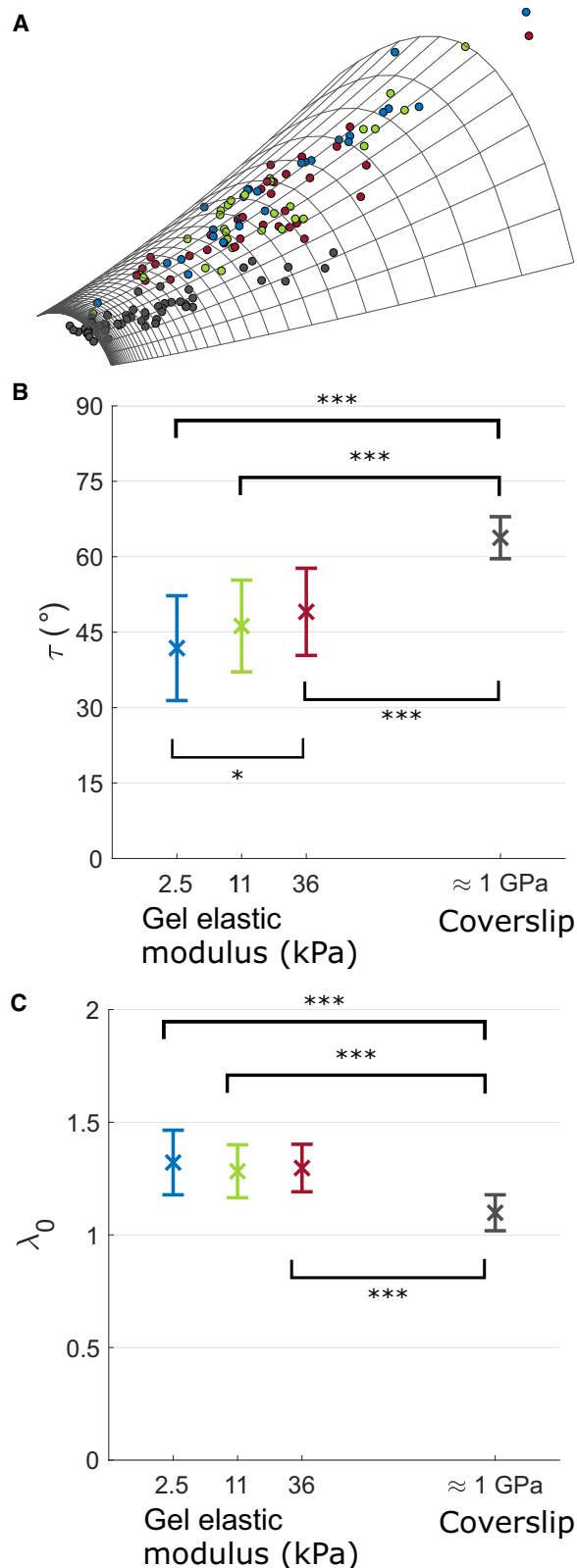


FIGURE 5 Changes in nondimensional parameters on varying elastic modulus of substrate. Huh7 cells were cultured on polyacrylamide gels with elastic modulus of 2.5, 11, and 36 kPa. By fitting our model to individual nuclei, nondimensional parameters λ_0 and τ were estimated. (A) Scatter

$$\gamma = 1.49$$

$$+ \sqrt[3]{(5.22Q - 4.46) + \sqrt{(5.22Q - 4.46)^2 + 1.95}}$$

$$+ \sqrt[3]{(5.22Q - 4.46) - \sqrt{(5.22Q - 4.46)^2 + 1.95}}. \quad (2)$$

Because γ is independent of λ_0 and a function of only τ (Fig. 6 A), τ can be obtained from γ using the graph shown in Fig. 6 C. It may be noted that Q is similar to Vogel number, which is a measure of the flatness of an object. Vogel number is defined as the ratio of the square root of the surface area to the cube root of the volume (33). Q is therefore proportional to the inverse of the cube of Vogel number.

We summarize the following techniques of increasing accuracy and complexity for estimating τ from nucleus shape.

- 1) From nuclear volume, V , and projected area, A , calculate $Q = (V\sqrt{\pi})/(2A^{3/2})$. Obtain the aspect ratio, γ , from Q by solving Eq. 1 or by using the expression in Eq. 2. Now, estimate τ from γ using the graph in Fig. 6 C. The points used to plot the graph in Fig. 6 C are given in the excel file “aspectratio_tau.xls” in Supporting materials and methods.
- 2) Assume a suitable value for R and estimate the normalized projected area, surface area, and volume of nuclei (see Materials and methods). Plot the normalized nuclear geometric parameters on the model surface and obtain the nondimensional parameters corresponding to the nearest grid point. MATLAB scripts and data files for performing this fit is given in the Supporting materials and methods.
- 3) Numerically fit the model by minimizing the error in normalized projected area, surface area, and volume between the simulated and experimentally measured nuclei (see Materials and methods).

Because our model has only two independent parameters, two geometric parameters, nuclear volume, and projected area, are sufficient to fit the model. Additional geometric parameters, such as surface area, ensure a better fit by correcting for any errors in the estimation of these nuclear shape measures. Hence, the first method using only two geometric parameters, volume, and projected area, should be employed only when the images are of high quality. We recommend signal to noise ratio >2 for this simplified method. We have derived this approximate

plot of nuclear shape parameters on the model surface. Each dot is an individual nucleus, and the colors represent the following items: black, control (coverslip ≈ 1 GPa, $N = 44$); blue, 2.5 kPa ($N = 23$); green, 11 kPa ($N = 28$); and red, 36 kPa ($N = 24$). Mean and standard deviation of τ and λ_0 are shown in (B) and (C), respectively. Statistical analysis was performed using ANOVA with Bonferroni correction and significance levels are represented by * $p < 0.05$, ** $p < 0.01$, and *** $p < 0.001$.

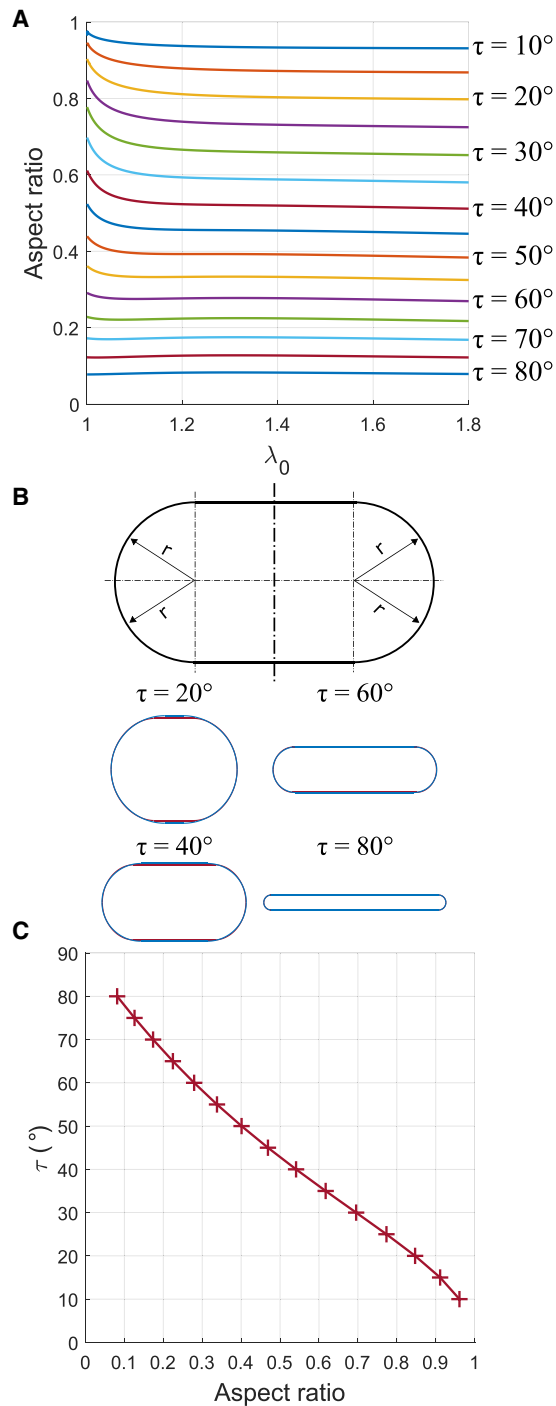


FIGURE 6 Geometric approximation of the model. (A) Variation of aspect ratio, height to diameter, of simulated nucleus shape with λ_0 for different values of τ . (B) Nucleus was approximated by an axisymmetric surface with cross section of a rectangle with semicircular ends. Comparison of approximation (blue) with simulated nuclei (red) for $\lambda_0 = 1.2$ and $\tau = 20^\circ, 40^\circ, 60^\circ$, and 80° . (C) τ for different values of aspect ratio obtained by fitting the approximate geometry to nuclear volume and projected area. To see this figure in color, go online.

method using nuclear volume and projected area because these geometric parameters can be easily obtained from high quality confocal images by thresholding.

DISCUSSION

We have shown that nuclear shapes can be represented by two independent nondimensional parameters τ and λ_0 , which can be geometrically interpreted as the flatness of the nucleus and isometric scaling or stretching of the nuclear envelope, respectively. Nuclei in a cell population have similar τ and variability predominantly along λ_0 . Changes in τ correlate with changes in actin tension. This was shown experimentally using multiple perturbations, biochemical and biomechanical, on multiple cell lines. Observations from previous studies independently corroborate with this relationship. Furthermore, we presented a method for conveniently estimating τ from nuclear volume and projected area using an analytical relationship and a graph.

After firmly establishing that τ correlates with actin tension, with further work that compares τ with actin tension measurements, it could be used as an alternative measure for actin tension. This would then be a convenient approach because measuring nuclear shape using confocal imaging is easier than conventional techniques for estimating actin tension through traction force microscopy (34,35). These techniques are cumbersome because they require live-cell imaging and specialized soft substrates such as polyacrylamide gels (34) and micropillars (35). However, they provide spatial distribution of traction force in units of force (N), stress (Pa) or energy (J), whereas τ is a single nondimensional number for a cell. Nevertheless, many studies might require only relative changes in actin tension between control and test samples, which are typically quantified using aggregate measures such as the strain energy (32), maximal force, root mean squared, or average stress (23). In such cases, τ estimated from nuclear shape could be a convenient alternative for estimating actin tension. Previously, a similar technique for indirectly inferring traction forces from cell shape was developed (36,37). It may be noted that decrease in actin tension cannot be detected from τ if the control cells have low tension. By using cytochalasin D treatment on cells with low tension (Figs. 3 D and S6) we have estimated this lower detection limit as $\tau \leq 30^\circ$. This restriction is because we have simplified the force from cortical actin to compression from a rigid flat plate. At low tension, this assumption may not be valid. Because we are observing only nuclear shape (dimension = length), our nondimensional parameters derived from nuclear geometry represent the ratio of force (dimension = $\text{kg}\cdot\text{m}\cdot\text{s}^{-2}$) to stiffness (dimension = $\text{kg}\cdot\text{s}^{-2}$). For instance, λ_0 and η_1 correspond to ratio between inflating pressure and elastic modulus. Therefore, these parameters may not be able to distinguish between an increase in inflating pressure and a decrease in elastic modulus.

In our previous work, we had used η_1 and η_2 to infer the changes in the expression of cytoskeletal and nuclear envelope proteins by hepatitis C virus (14). Here, we found that

these two nondimensional parameters are correlated under all perturbations done in this study (Figs. S5, S8, and S10). This could be because of molecular mechanisms interrelating osmotic pressure and actin tension (38). In contrast, the other set of nondimensional parameters, λ_0 and τ , correspond to the principal directions of variability and are independent of each other. This independence can be inferred from the orthogonality of the contour lines for λ_0 and τ in Fig. 1 D. The values of λ_0 and τ estimated from the nuclei of a cell population are uncorrelated (Fig. S2 B), further confirming that these parameters are independent. Another important feature of τ is that it is independent of R , the radius of the nucleus in the reference configuration (Fig. 1 B). This is a very important property because the undeformed configuration is unobservable. Having to assume this unobservable undeformed state is a fundamental drawback of biomechanics studies that employ a solid mechanics approach. The independence with the initial configuration allows us to define a lower limit, $\tau > 30^\circ$, for detecting a reduction in actin tension. Even though η_2 varies analogous to τ (compare Figs. 3, 4, and 5 with Figs. S5, S8, and S10), we cannot define a lower limit of detection for η_2 because it depends on the value chosen for R . Therefore, we recommend τ and λ_0 for describing nuclear shape and its relationship with mechanical factors of the cell such as the cytoskeleton and nuclear envelope.

We showed that nucleus morphology in a cell population is primarily a single-variable function of λ_0 . The variability in τ accounts for less than 25% of the total variability in nuclear shape. This means that nuclei in a cell population have uniform flatness and the variability in size is due to isometric scaling. This univariate behavior is surprising because of multiple biomechanical and biochemical parameters that are known to govern nuclear shape. In our model we have considered the following biomechanical parameters: tension in cortical actin, elastic modulus of the nuclear envelope, and osmotic pressure difference between the nucleoplasm and cytoplasm, which are dependent on the following biochemical parameters: expression of actin, myosin, and lamin. The univariate behavior of nucleus shape suggests that these biomechanical and biochemical parameters collapse into a single parameter through interdependent signaling mechanisms. For example, lamin-A,C is known to regulate myosin through the SRF pathway (20). Furthermore, because the principal variability is along λ_0 , which is equivalent to scaling, this variability could be cell-cycle dependent. This is because cell cycle progression is known to increase nuclear size to accommodate the increasing DNA content (39). A cell-cycle-dependent mechanism can also explain the variability in τ because traction forces, and therefore the actin tension, is known to vary with cell cycle (40). Therefore, the variability in nuclear shapes could be arising out of a cell-cycle-dependent mechanism with biochemical feedback to integrate all the independent variables to a single variable.

Our results show that independent mechanisms for modulating actin tension, biochemical, or biomechanical, produce similar changes in nuclear shape. Increasing tension flattens the nucleus, increasing τ and vice versa. This suggests that the connection between the actin tension and nucleus shape is essentially mechanical. The emerging mechanical picture for a cell is akin to a tent: stabilized by the actin tension (similar to the tensed canopy), and supported by the nucleus (akin to the pole that carries compression). The nuclear envelope acquires compression-carrying capacity through a net inflating pressure that tenses it, akin to a balloon. Because the structure is stabilized by the tensions in cortical actin and nuclear envelope, this mechanical viewpoint is akin to a tensegrity with the following distinctions from the original tensegrity theory for cells (41): 1) the tensile element is a two-dimensional membrane 2) primary compression-carrying member is the nucleus, which is an inflated membrane, and therefore a tensegrity by itself. Our study shows that this simple mechanical picture satisfies multiple independent experimental observations.

In summary, we have used a mechanical model to decompose the contributions from actin tension and elastic modulus of the nuclear envelope to nuclear shape. The nondimensional parameters τ and λ_0 that correlate with these physical properties of the cell, were shown to be the principal variables along which nuclear shape varies in a cell population. By validating our model with multiple perturbations across many cell lines and previous studies, we propose a mechanical picture of the cell akin to a tent, which is stabilized by the tensions in actin cytoskeleton and nuclear envelope. We further derive a convenient method to estimate τ from nuclear volume and projected area and thereby pave the way for predicting the actin tension from nuclear shape with further work and experimental data. From a larger perspective, our results show that deeper physical insights can be derived by combining physical principles with experimental observations.

SUPPORTING MATERIAL

Supporting material can be found online at <https://doi.org/10.1016/j.bpj.2021.09.035>.

AUTHOR CONTRIBUTIONS

S.B. and G.K.A. designed the research. S.R.R., A.B., and R.P.P. performed the experiments. S.B. performed the computations and analyzed the data. S.B. and G.K.A. wrote the article.

ACKNOWLEDGMENTS

Authors would like to thank Suma S. Mathad for the preliminary experiments, Sachin Arya for the illustrations and the BBI2 grant from the Department of Biotechnology, Government of India for funding.

REFERENCES

1. Enyedi, B., M. Jelcic, and P. Niethammer. 2016. The cell nucleus serves as a mechanotransducer of tissue damage-induced inflammation. *Cell*. 165:1160–1170.
2. Thomas, C. H., J. H. Collier, ..., K. E. Healy. 2002. Engineering gene expression and protein synthesis by modulation of nuclear shape. *Proc. Natl. Acad. Sci. USA*. 99:1972–1977.
3. Irianto, J., C. R. Pfeifer, ..., D. E. Discher. 2016. Nuclear lamins in cancer. *Cell. Mol. Bioeng*. 9:258–267.
4. de Las Heras, J. I., D. G. Batrakou, and E. C. Schirmer. 2013. Cancer biology and the nuclear envelope: a convoluted relationship. *Semin. Cancer Biol.* 23:125–137.
5. Lammerding, J., P. C. Schulze, ..., R. T. Lee. 2004. Lamin A/C deficiency causes defective nuclear mechanics and mechanotransduction. *J. Clin. Invest.* 113:370–378.
6. Worman, H. J., C. Ostlund, and Y. Wang. 2010. Diseases of the nuclear envelope. *Cold Spring Harb. Perspect. Biol.* 2:a000760.
7. Folker, E. S., C. Ostlund, ..., G. G. Gundersen. 2011. Lamin A variants that cause striated muscle disease are defective in anchoring transmembrane actin-associated nuclear lines for nuclear movement. *Proc. Natl. Acad. Sci. USA*. 108:131–136.
8. Kim, D.-H., B. Li, ..., S. X. Sun. 2015. Volume regulation and shape bifurcation in the cell nucleus. *J. Cell Sci.* 128:3375–3385.
9. Ramdas, N. M., and G. V. Shivashankar. 2015. Cytoskeletal control of nuclear morphology and chromatin organization. *J. Mol. Biol.* 427:695–706.
10. Irianto, J., J. Swift, ..., D. A. Lee. 2013. Osmotic challenge drives rapid and reversible chromatin condensation in chondrocytes. *Biophys. J.* 104:759–769.
11. Lovett, D. B., N. Shekhar, ..., T. P. Lele. 2013. Modulation of nuclear shape by substrate rigidity. *Cell. Mol. Bioeng*. 6:230–238.
12. Buxboim, A., J. Irianto, ..., D. E. Discher. 2017. Coordinated increase of nuclear tension and lamin-A with matrix stiffness outcompetes lamin-B receptor that favors soft tissue phenotypes. *Mol. Biol. Cell*. 28:3333–3348.
13. Feng, W. W., and W. H. Yang. 1973. On the contact problem of an inflated spherical nonlinear membrane. *J. Appl. Mech.* 45:209–214.
14. Balakrishnan, S., S. S. Mathad, ..., G. K. Ananthasuresh. 2019. A nondimensional model reveals alterations in nuclear mechanics upon hepatitis C Virus replication. *Biophys. J.* 116:1328–1339.
15. Tse, J. R., and A. J. Engler. 2010. Preparation of hydrogel substrates with tunable mechanical properties. *Curr. Protoc. Cell Biol.* 47:10.16.1–10.16.16.
16. Cao, X., E. Moendarbary, ..., V. B. Shenoy. 2016. A chemomechanical model for nuclear morphology and stresses during cell transendothelial migration. *Biophys. J.* 111:1541–1552.
17. Rowat, A. C., J. Lammerding, and J. H. Ipsen. 2006. Mechanical properties of the cell nucleus and the effect of emerin deficiency. *Biophys. J.* 91:4649–4664.
18. Coleman, T. F., and Y. Li. 1994. On the convergence of interior-reflective Newton methods for nonlinear minimization subject to bounds. *Math. Program.* 67:189–224.
19. Velliste, M., and R. F. Murphy. 2002. Automated determination of protein subcellular locations from 3D fluorescence microscope images. In *Proceedings IEEE International Symposium on Biomedical Imaging*, IEEE, pp. 867–870.
20. Buxboim, A., J. Swift, ..., D. E. Discher. 2014. Matrix elasticity regulates lamin-A,C phosphorylation and turnover with feedback to actomyosin. *Curr. Biol.* 24:1909–1917.
21. Alisafaei, F., D. S. Jokhun, ..., V. B. Shenoy. 2019. Regulation of nuclear architecture, mechanics, and nucleocytoplasmic shuttling of epigenetic factors by cell geometric constraints. *Proc. Natl. Acad. Sci. USA*. 116:13200–13209.
22. Danowski, B. A. 1989. Fibroblast contractility and actin organization are stimulated by microtubule inhibitors. *J. Cell Sci.* 93:255–266.
23. Rape, A., W. H. Guo, and Y. L. Wang. 2011. Microtubule depolymerization induces traction force increase through two distinct pathways. *J. Cell Sci.* 124:4233–4240.
24. Kolodney, M. S., and E. L. Elson. 1995. Contraction due to microtubule disruption is associated with increased phosphorylation of myosin regulatory light chain. *Proc. Natl. Acad. Sci. USA*. 92:10252–10256.
25. Verin, A. D., A. Birukova, ..., J. G. N. Garcia. 2001. Microtubule disassembly increases endothelial cell barrier dysfunction: role of MLC phosphorylation. *Am. J. Physiol. Lung Cell. Mol. Physiol.* 281:L565–L574.
26. Birukova, A. A., K. Smurova, ..., A. D. Verin. 2004. Microtubule disassembly induces cytoskeletal remodeling and lung vascular barrier dysfunction: role of Rho-dependent mechanisms. *J. Cell. Physiol.* 201:55–70.
27. Chang, Y.-C., P. Nalbant, ..., G. M. Bokoch. 2008. GEF-H1 couples nocodazole-induced microtubule disassembly to cell contractility via RhoA. *Mol. Biol. Cell*. 19:2147–2153.
28. Discher, D. E., P. Janmey, and Y.-L. Wang. 2005. Tissue cells feel and respond to the stiffness of their substrate. *Science*. 310:1139–1143.
29. Li, Q., A. Kumar, ..., G. V. Shivashankar. 2014. The regulation of dynamic mechanical coupling between actin cytoskeleton and nucleus by matrix geometry. *Biomaterials*. 35:961–969.
30. Damodaran, K., S. Venkatachalapathy, ..., G. V. Shivashankar. 2018. Compressive force induces reversible chromatin condensation and cell geometry-dependent transcriptional response. *Mol. Biol. Cell*. 29:3039–3051.
31. Merkher, Y., M. B. Alvarez-Elizondo, and D. Weihs. 2017. Taxol reduces synergistic, mechanobiological invasiveness of metastatic cells. *Converg. Sci. Phys. Oncol.* 3:044002.
32. Prah, L. S., P. F. Bangasser, ..., D. J. Odde. 2018. Microtubule-based control of motor-clutch system mechanics in glioma cell migration. *Cell Rep.* 25:2591–2604.e8.
33. Vogel, S. 2013. *Comparative Biomechanics: Life's Physical World*. Princeton University Press, Princeton, NJ.
34. Dembo, M., and Y. L. Wang. 1999. Stresses at the cell-to-substrate interface during locomotion of fibroblasts. *Biophys. J.* 76:2307–2316.
35. Tan, J. L., J. Tien, ..., C. S. Chen. 2003. Cells lying on a bed of micro-needles: an approach to isolate mechanical force. *Proc. Natl. Acad. Sci. USA*. 100:1484–1489.
36. Brodland, G. W., V. Conte, ..., M. Miodownik. 2010. Video force microscopy reveals the mechanics of ventral furrow invagination in *Drosophila*. *Proc. Natl. Acad. Sci. USA*. 107:22111–22116.
37. Chiou, K. K., L. Hufnagel, and B. I. Shraiman. 2012. Mechanical stress inference for two dimensional cell arrays. *PLoS Comput. Biol.* 8:e1002512.
38. Di Ciano, C., Z. Nie, ..., A. Kapus. 2002. Osmotic stress-induced remodeling of the cortical cytoskeleton. *Am. J. Physiol. Cell Physiol.* 283:C850–C865.
39. Fidorra, J., T. Mielke, ..., L. E. Feinendegen. 1981. Cellular and nuclear volume of human cells during the cell cycle. *Radiat. Environ. Biophys.* 19:205–214.
40. Vianay, B., F. Senger, ..., M. Théry. 2018. Variation in traction forces during cell cycle progression. *Biol. Cell*. 110:91–96.
41. Ingber, D. E. 1993. Cellular tensegrity: defining new rules of biological design that govern the cytoskeleton. *J. Cell Sci.* 104:613–627.